Precision Position Control of the DelFly II Flapping-wing Micro Air Vehicle in a Wind-tunnel

T. Cunis*, M. Karásek, and G.C.H.E. de Croon
Delft University of Technology, Kluyverweg 1, Delft, The Netherlands

Abstract

Flapping-wing MAVs represent an attractive alternative to conventional designs with rotary wings, since they promise a much higher efficiency in forward flight. However, further insight into the flapping-wing aerodynamics is still needed to get closer to the flight performance observed in natural fliers. Here we present the first step necessary to perform a flow visualization study of the air around the flapping wings of a DelFly II MAV *in-flight*: a precision position control of flight in a wind-tunnel. We propose a hierarchical control scheme implemented in the open-source Paparazzi UAV autopilot software. Using a decoupling, combined feed-forward and feed-back control approach as a core, we were able to achieve a precision of $\pm 2.5\,\mathrm{cm}$ for several seconds, which is much beyond the requirements for a time resolved stereo PIV technique.

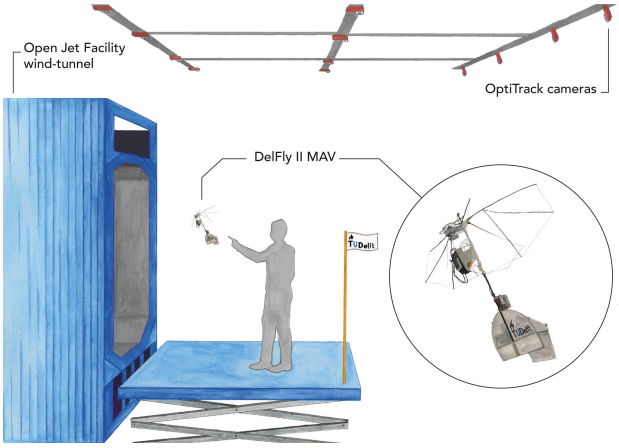

Figure 1: The DelFly II preforming a precision flight in the wind-tunnel. The achieved precision of $\pm 2.5\,\mathrm{cm}$ will allow unprecedented *in-flight* aerodynamic measurements in future. *Commissioned illustration by Sarah Gluschitz, licensed under CC BY-ND.*

1 Introduction

The recent boom of Micro Air Vehicles (MAVs) has induced a deep interest in flapping flight. At the scales of insects and small birds, flapping-wing MAVs are expected to challenge conventional rotorcraft designs by combining precision and agility at hover with energy efficient cruising flight. However, their development is still at the beginning and even the performance of state-of-the-art designs [1–3] remains far behind their biological counterparts. One of the reasons of this gap is our limited understanding of the complex and unsteady aerodynamic mechanisms occurring during flapping.

Numerical modelling of flapping wings can provide some insight; nevertheless, it remains a challenge on its own. Despite an intense research in recent years [4, 5], the existing models still struggle to match empirical data consistently. Thus, experimental techniques remain the most suitable tool for studying flapping flight.

So far, most experiments have been carried out in a tethered configuration where the aerodynamic forces and moments can be measured directly, in natural fliers [6] as well as in MAVs [7, 8]. However, it remains debatable whether these measurements are representative of free-flight conditions, especially in animals that behave abnormally when their body motion is restrained. A possible contamination of tethered measurements by structural vibrations was also reported in MAVs when compared to free flight estimates [9].

Another experimental tool used for studying flapping flight are flow visualization techniques. Particle Image Velocimetry (PIV) was used to capture the flow patterns around and behind man-made flapping wings in a tethered configuration [10–13] and also in various natural fliers flying in a wind-tunnel [14–16]. Nevertheless, such measurements always include a random factor due to unpredictable behaviour of even a well trained animal. Free flight PIV measurements with man made flappers have not yet been tried, but could bring much more consistent data as their manoeuvres can be pre-programmed.

Here, we present a first necessary step towards a free-flight PIV measurement on a flapping-wing MAV: a precision autonomous flight in a wind-tunnel (Fig. 1), something that has not yet been tried in flapping-wing MAVs apart from the DelFly platform itself [17]. Even for other platforms (fixed-wings, multi-rotors), only a few examples of autonomous wind-tunnel flying can be found in the literature [18, 19].

So far, most research on flapping flight control focused on tail-less designs that require active attitude stabilization to

*T. Cunis was MSc candidate at RWTH Aachen University. Authors' email addresses: torbjoern.cunis@wtnet.de; m.karasek@tudelft.nl; g.c.h.e.decroon@tudelft.nl

stay in the air, e.g. [20–22]; this is not needed in tailed designs, like the DelFly, that benefit from passive stability. The higher level (guidance) control has deserved much less attention, e.g. in GPS-based flying [23]; however, very good trajectory tracking performance was achieved with a tethered, but unconstrained, insect-sized tail-less RoboBee [24]. Despite the lack of an accurate robot model, a Root Mean Square (RMS) error of $1\,\mathrm{cm}$ ($\approx 30\,\%$ of its wingspan) was achieved in hovering and near-hover trajectory tracking flights lasting several seconds with a single loop adaptive flight control. Including the Iterative Learning Control algorithm, which learns the robot dynamics uncaptured by the model, allowed to track also more aggressive manoeuvres [25].

Nevertheless, the DelFly differs significantly from the RoboBee: it is a tailed, passively stable platform designed primarily for (slow) forward flight. It has no (direct) roll control authority and a significant coupling exists between the pitch angle and vertical dynamics due to gliding effects. Also, no aggressive manoeuvres are needed for the intended tests. Thus, we adopted a rather classical approach with a cascaded structure, enhanced with a speed-thrust control block to deal with the longitudinal coupling effects and an adaptation phase to compensate for the model errors. Compared to the previous tests [17], we further improved the position sensing by using a commercial external motion tracking system.

In this paper, we first introduce the experimental setup in Section 2. The main contribution of this work is the control approach described in Section 3. The test results are presented and discussed in Section 4, which is followed by Section 5 with the conclusion.

2 Experimental Setup

2.1 DelFly II MAV

The flapping-wing MAV used in the experiments described here is the DelFly II (Fig. 2, further called the DelFly), which is a well studied platform that has been developed by the TU Delft for over ten years [3, 26]. The DelFly has two flexible wings flapping in cross configuration; its characteristic wing motion with lift enhancing *clap-and-peel* mechanism is displayed in Fig 3.

The MAV is stabilized and controlled by a conventional tail with horizontal and vertical stabilizers and two actuated control surfaces; the elevator deflection results in a pure pitch moment, the rudder generates a combined roll and yaw moment.

The DelFly is equipped with a Lisa/S autopilot board [27], which includes a 6 DOF MEMS IMU for attitude estimation and an MCU running the Paparazzi UAV software[1]. Further on-board components include a DelTang Rx31 receiver and an ESP8266 Esp-09 WiFi module for data uplink and telemetry downlink. Four active, infra-red LED markers are placed at the nose, fin, at the tailplane (2x), forming a rotational asymmetric tetrahedron; thus, attitude and position of its geometrical centre can be uniquely recognized by the tracking system. In the current implementation, the controller uses the position and heading information from the tracking system and estimates roll and pitch angle from the on-board IMU.

[1] https://wiki.paparazziuav.org

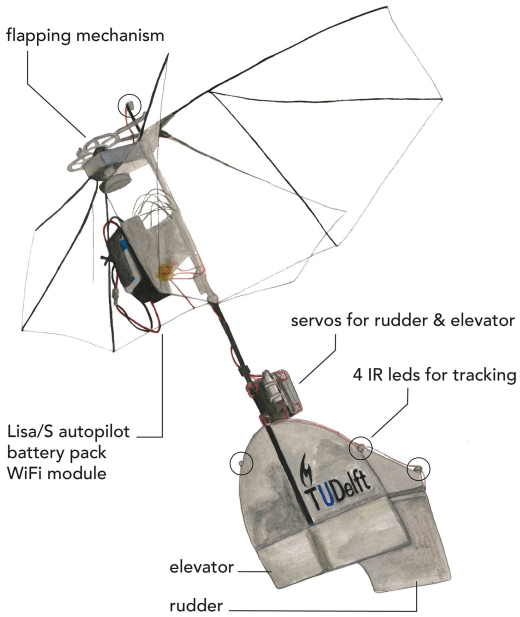

Figure 2: The DelFly II flapping-wing MAV used in this study. *Commissioned illustration by Sarah Gluschitz, licensed under CC BY-ND.*

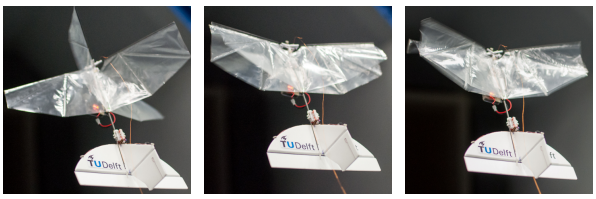

(a) (b) (c)

Figure 3: Three important phases of the DelFly MAV flapping cycle: (a) wings fully opened, (b) wings clapping, (c) wings peeling apart.

2.2 Wind-tunnel set-up

The tests presented here were carried out in the *Open Jet Facility* of TU Delft. This close-circuit low-speed wind-tunnel offers an open test section of nearly $3\,\mathrm{m} \times 3\,\mathrm{m}$ and is thus greatly suitable for MAV free-flight experiments. The wind speed, controlled by the wind-tunnel software via the fan rpm, can reach up to $35\,\mathrm{m/s}$. We have noticed that the wind speed control was not very accurate at very low speeds, where our tests were performed (0.5 to $1.5\,\mathrm{m/s}$), resulting in a steady state error. Thus, in the results we will state the wind

speed set-point V_W^{SP} rather than the (unknown) actual speed V_W.

The DelFly has been tracked by twelve motion tracking cameras (OptiTrack Flex 13, NaturalPoint, Inc.) attached at the ceiling of the wind-tunnel room (Fig. 1), providing the MAV position and orientation at a rate of up to 120 Hz with a mean error of $\approx 0.2\,\mathrm{mm}$ per marker. The position and heading were sent on-board at a rate of 30 Hz, via the Paparazzi Ground Control Station, using the WiFi datalink.

2.3 Axis systems

We are using the axis systems defined by ISO 1151-1 and -2, see Fig. 4. In addition to the usual geographic, flight-path, air-path, and body-fixed axis systems, we introduce the *wind-tunnel reference system* in order to define the (desired) motion in the wind-tunnel: the x_w-axis points opposite the wind velocity vector, z_w points down and y_w completes the right-handed Cartesian system. As the origin is located at the geographic system's origin, the wind-tunnel reference system differs from the geographic only by rotation.

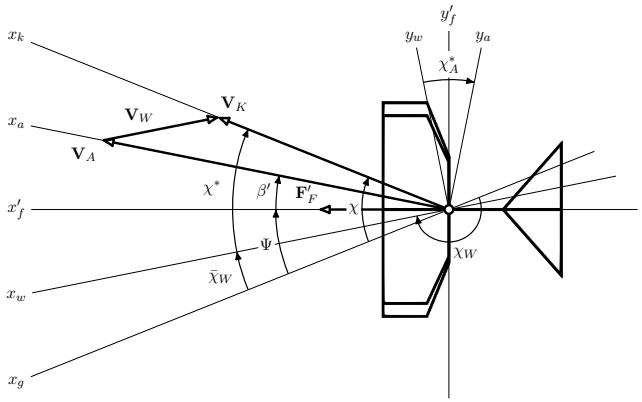

Figure 4: Axes of the horizontal flight dynamics. Projections of axes or quantities into the drawing layer are marked by $\odot'$. *Based upon [28].*

The body-fixed coordinate system is defined by the body's main axes: the x_f-axis points along the fuselage towards the nose, the z_f-axis points opposite to the direction of the vertical stabilizer, and the y_f-axis pointing starboard completes the right-handed system. Its origin is placed at the centre of the tracked body (defined by the four LED markers), which we assume to be close enough to the centre of mass.

3 CONTROL APPROACH

For the problem of precision position control we propose a hierarchic control scheme according to Fig. 5. In contrast to the classical flight-control hierarchy, an additional *speed-thrust control* block was inserted between attitude and guidance control to deal with the coupling of lift and thrust, induced by varying effects of flapping and gliding at different flight speeds.

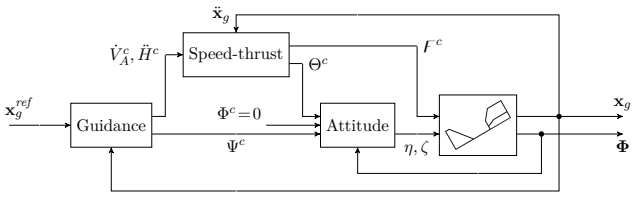

Figure 5: The hierarchic control scheme for the DelFly control approach.

In the longitudinal x_a-z_a-plane, the motion is determined by the air-speed V_A and the change in height $\dot{H}$. For the speed-thrust controller, we make the following assumptions about the flight condition of the DelFly:

- the air-speed vector lies in the horizontal plane;
- the thrust vector is aligned with the air-speed.

These assumptions are fully satisfied in steady-state flight in the wind-tunnel, and sufficiently met for slight deviations from the set-point.

3.1 Guidance control

Flying in the wind-tunnel, the direction of the aircraft velocity $\vec{\mathbf{V}}_A$ is (in steady-state) pointing opposite the wind velocity vector $\vec{\mathbf{V}}_W$, that is we have $\vec{\mathbf{V}}_A = -\vec{\mathbf{V}}_W$ and there is no motion relative to ground ($\vec{\mathbf{V}}_K = \vec{\mathbf{V}}_A + \vec{\mathbf{V}}_W = \mathbf{0}$, see Fig. 4). As the wind-direction is constant, we introduce the non-rotating wind-tunnel reference axis system $[x_w, y_w, z_w]$ opposing wind azimuth χ_W and note the angle between normal earth-fixed x_g-axis and wind-tunnel reference x_w-axis, clockwise positive, by $\bar{\chi}_W = \chi_W - \pi$.

The guidance control approach presented here is based on non-linear dynamic inversion [29]. Dynamic inversion control enjoys the benefits of directly injecting the desired closed-loop system behaviour, *i.e.* the coefficients of the characteristic polynomials, via the control law. In the axes of the wind-tunnel reference system, assuming constant wind speed ($\dot{V}_W = 0$), we end up with the following component-wise accelerations in steady-state flight:

$$\ddot{x}_w = \dot{V}_A - \dot{V}_W = \dot{V}_A \tag{1}$$

$$\ddot{y}_w = m^{-1}\left(F_F \sin(\Psi - \bar{\chi}_W) - F_D \sin(\chi_A - \bar{\chi}_W)\right) \tag{2}$$

$$\ddot{z}_w = -\ddot{H}. \tag{3}$$

For small angles $\Psi - \bar{\chi}_W$ and $\chi_A - \bar{\chi}_W$, the lateral equation reduces to

$$\ddot{y}_w = m^{-1} F_F \left(\Psi - \bar{\chi}_W\right). \tag{4}$$

Using $\dot{V}_A$, $\ddot{H}$, and Ψ as commands to the underlying control loops we have the control laws

$$\dot{V}_A^c = \nu_x \tag{5}$$

$$\Psi^c = \lambda_{\Psi\ddot{y}} \nu_y + \bar{\chi}_W \tag{6}$$

$$\ddot{H}^c = \nu_z, \tag{7}$$

where the lateral ratio $\lambda_{\Psi\ddot{y}}$ is introduced to cancel $m^{-1}F_F$ in Eq. 4. The pseudo-commands are given by

$$\nu_x = d_{\dot{V}_A x_w}\Delta\dot{x}_w + k_{\dot{V}_A x_w}\Delta x_w \tag{8}$$

$$\nu_y = d_{\ddot{y}_w y_w}\Delta\dot{y}_w + k_{\ddot{y}_w y_w}\Delta y_w + i_{\ddot{y}_w y_w}\int \Delta y_w \,\mathrm{d}t \tag{9}$$

$$\nu_z = d_{\ddot{H} z_w}\Delta\dot{z}_w + k_{\ddot{H} z_w}\Delta z_w, \tag{10}$$

where $i_{\ddot{y}_w y_w}$ is a lateral integral gain added to correct steady-state offsets in the heading controller. Thus, the closed loop systems resemble second-order behaviour. The lateral integral gain $i_{\ddot{y}_w y_w}$ and ratio $\lambda_{\Psi\ddot{y}_w}$ have been tuned in the wind-tunnel.

3.2 Speed-thrust control

Controlling the behaviour in the longitudinal plane is the core task of the designed controller. Since the generation of lift and thrust is highly coupled, the speed-thrust control law needs to command a suitable combination of pitch angle and flapping frequency. In Fig. 6, the overall control strategy is shown: pitch angle and throttle are commanded by a forward control block from the forward and vertical acceleration set-points, which are being adjusted by the feedback loop.

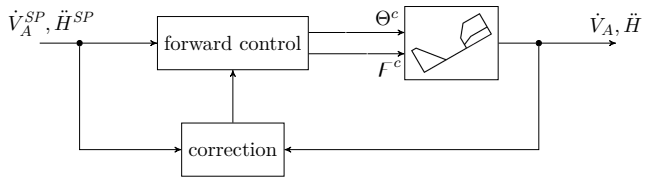

Figure 6: The overall control strategy for speed-thrust control.

Forward control Using static wind-tunnel measurements for different wind speeds, pitch angles, and throttle commands [30], a linear relationship between thrust F_F , lift F_L and pitch angle Θ and throttle F was found by first-oder Taylor linearisation:

$$\begin{bmatrix} F_F \\ F_L \end{bmatrix} = \begin{bmatrix} F_F(\Theta_0, F_0, V_W) \\ F_L(\Theta_0, F_0, V_W) \end{bmatrix} + \mathbf{F}_{\text{Æ}}(V_W) \begin{bmatrix} \Delta\Theta \\ \Delta F \end{bmatrix}, \tag{11}$$

where Θ_0, F_0 denote the condition of no acceleration (equilibrium) and $\mathbf{F}_{\text{Æ}}$ the matrix of force gradients at the equilibrium; the lift and thrust force in equilibrium is $F_{F0} = F_{D0}(V_W)$ and $F_{L0} = F_G$.

Considering our initial assumption ($\Delta F_F = m\dot{V}_A, \Delta F_L = m\ddot{H}$), we obtain a wind speed-dependent forward control law by inversion of Eq. 11 as

$$\begin{bmatrix} \Theta^c \\ F^c \end{bmatrix} = \begin{bmatrix} \Theta_0 \\ F_0 \end{bmatrix} + m\mathbf{F}_{\text{Æ}}^{-1} \begin{bmatrix} \dot{V}_A^{SP} \\ \ddot{H}^{SP} \end{bmatrix} \tag{12}$$

As $\mathbf{F}_{\text{Æ}}$ has been derived for different wind speeds, our forward control law follows a *gain scheduling* approach.

Feedback correction In feedback loop, we employ a simple PI control law in order to correct model uncertainties and reject disturbances

$$\begin{bmatrix} \dot{V}_A^{\text{fb}} \\ \ddot{H}^{\text{fb}} \end{bmatrix} = k \begin{bmatrix} \Delta\dot{V}_A \\ \Delta\ddot{H} \end{bmatrix} + i \int \begin{bmatrix} \Delta\dot{V}_A \\ \Delta\ddot{H} \end{bmatrix} \mathrm{d}t, \tag{13}$$

where the integrated error can be calculated as $\int \Delta\dot{V}_A \,\mathrm{d}t = \int \dot{V}_A^{SP} \,\mathrm{d}t - V_A$; $\int \Delta\ddot{H} \,\mathrm{d}t = \int \ddot{H}^{SP} \,\mathrm{d}t - \dot{H}$.

As $\mathbf{F}_{\text{Æ}}^{-1}$ features a guess of direction of the force gradients, we add the correction *before* the forward control; thus, the combined forward-backward control law results into

$$\begin{bmatrix} \Theta^c \\ F^c \end{bmatrix} = \begin{bmatrix} \Theta_0 \\ F_0 \end{bmatrix} + m\mathbf{F}_{\text{Æ}}^{-1}\Big(\begin{bmatrix} \dot{V}_A^{SP} \\ \ddot{H}^{SP} \end{bmatrix} + k \begin{bmatrix} \Delta\dot{V}_A \\ \Delta\ddot{H} \end{bmatrix} + i \int \begin{bmatrix} \Delta\dot{V}_A \\ \Delta\ddot{H} \end{bmatrix}\Big). \tag{14}$$

3.3 Semi-adaptive control approach

The combined forward-backward controller, as presented so far, compensates model errors in both force gradients and equilibrium conditions by feedback. We enhance the control approach by a quasi-adaptation stage to initially adapt to the equilibrium condition (Θ_0, F_0); we call this extended approach *semi-adaptive*.

First, we can use a position feedback to find the "true" equilibrium condition, without de-stabilizing the system:

Lemma 1. *Let $\hat{\Theta}_0$, $\hat{F}_0$, and $\hat{\mathbf{F}}_{\text{Æ}}$ be close guesses of the pitch angle, throttle command, and matrix of force gradients at equilibrium, respectively. Given an initial longitudinal position (x_{w0}, H_0) and a feedback law*

$$\begin{bmatrix} \Theta^c \\ F^c \end{bmatrix} = \begin{bmatrix} \hat{\Theta}_0 \\ \hat{F}_0 \end{bmatrix} + m\hat{\mathbf{F}}_{\text{Æ}}^{-1}\gamma \begin{bmatrix} x_{w0} - x_w \\ H_0 - H \end{bmatrix}, \tag{15}$$

for a suitable gain $\gamma \in \mathbb{R}_{>0}$ it holds

1. *there is a position (x'_w, H') close to (x_{w0}, H_0) where the equilibrium condition is met;*
2. *in the neighbourhood of (x'_w, H') this position will be approached.*

Proof. See Appendix. □

That is, the stable position (x'_w, H') is approached and Eq. 15 yields the true pitch angle $\Theta_0 = \Theta^c(x'_w, H')$ and throttle command $F_0 = F^c(x'_w, H')$.

We now split our control approach into two subsequent stages: *adaptation* and *correction*, see Fig. 7. First, the position feedback of Eq. 15 stabilizes the position; as soon as the equilibrium is found by Lemma 1 (time t_A), the controller switches to the correction stage (and remains here).

3.4 Attitude control

We use elevator and rudder of the DelFly to control pitch angle and heading, respectively. While roll is also affected by the rudder, it quickly returns to zero thanks to passive stability. We employ standard PID feedback and use directly the error in rates for the derivative part.

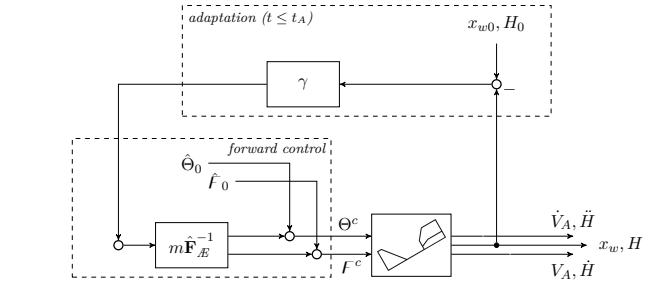

(a) Adaptation stage, $t \leq t_A$.

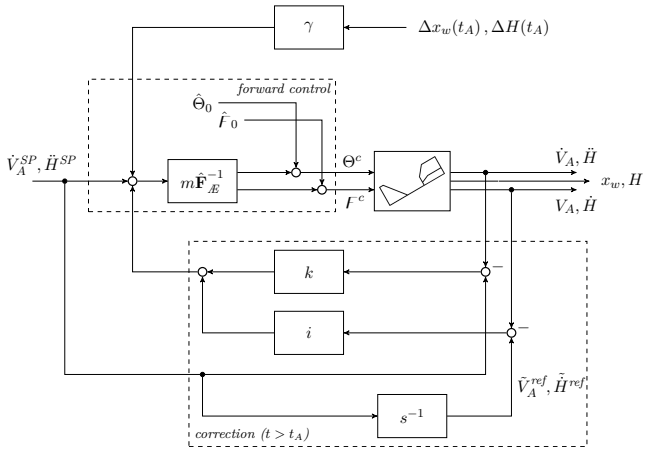

(b) Correction stage, $t > t_A$.

Figure 7: The two-stage semi-adaptive control approach: at time $t = t_A$, the semi-adaptive controller switches from the adaptation (a) to the correction (b) stage.

4 Results

If not stated otherwise, the wind-tunnel speed controller was set to $V_W^{SP} = 0.8\,\mathrm{m/s}$. Because the wind speed measurement was not available on-board, the wind tunnel set point speed was used instead to choose the forward gains of the speed-thrust controller.

4.1 Precision in steady-state

The steady state results are shown in Fig. 8. We achieved the highest steady-state precision using only an integral gain $i = 300\,\%$ in the correction stage. The control precision in the vertical direction was around $\pm 1.0\,\mathrm{cm}$, except for a disturbance around time $t = 140\,\mathrm{s}$. The precision in the forward axis was around $\pm 2.5\,\mathrm{cm}$.

The performance in the lateral axis is not influenced by the integral gain but heavily oscillating; thus, a lateral precision of $\pm 5.0\,\mathrm{cm}$ is achieved most of the time. We further discuss the lateral results in Section 4.2.

The RMS error over the time interval displayed in Fig. 8 (approx. $150\,\mathrm{s}$) was $0.9\,\mathrm{cm}$, $1.7\,\mathrm{cm}$ and $3.2\,\mathrm{cm}$ for vertical, forward and lateral direction, respectively.

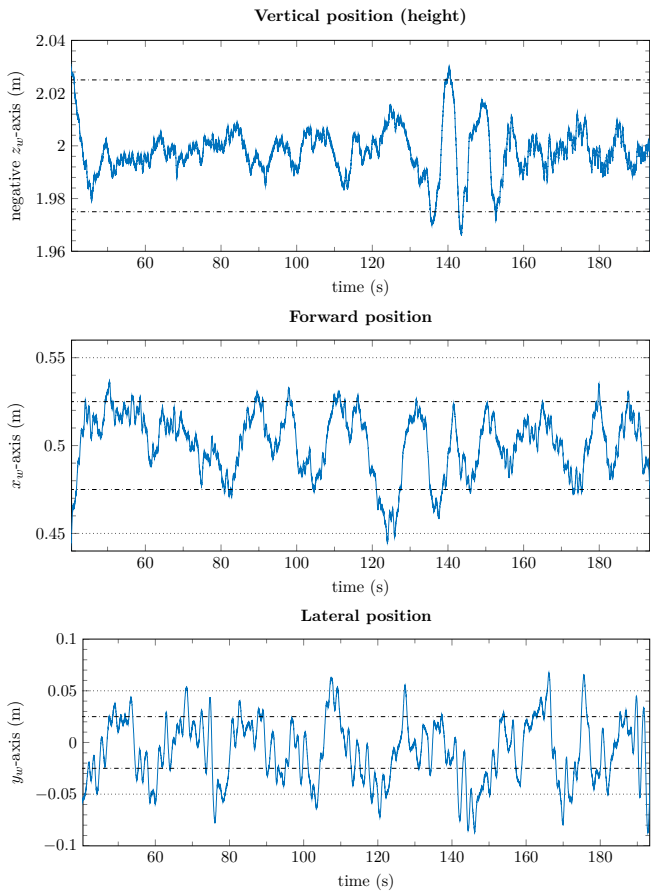

Figure 8: Steady-state position (by OptiTrack); dashed and dotted lines are indicating $\pm 2.5\,\mathrm{cm}$ and $\pm 5.0\,\mathrm{cm}$, respectively. (*wind speed* $V_W^{SP} = 0.8\,\mathrm{m/s}$*; semi-adaptive speed-thrust control with* $k = 0$*,* $i = 300\,\%$.)

4.2 Robustness to wind speed

While flying, we increased the wind speed set-point stepwise from 0.7 up to $1.3\,\mathrm{m/s}$ (Fig. 9); neither forward nor feedback gains were changed during this test.

In the vertical and forward axes, the control approach is clearly robust and the precision remains unaffected. As one can see from the RMS error in Tab. 1, the accuracy is even increasing slightly with the wind speed.

V_W^{SP}	$0.7\,\mathrm{m/s}$	$1.0\,\mathrm{m/s}$	$1.3\,\mathrm{m/s}$
RMS z_w (cm)	1.35	1.10	0.90
RMS x_w (cm)	3.26	2.47	2.25
RMS y_w (cm)	3.44	5.52	9.22

Table 1: RMS position error for different wind speeds.

The precision in lateral axis, however, deteriorates for increasing wind speed; so does the RMS error. Since the rudder is more effective in low-pitch, fast-forward flight and a change of heading induces an increased lateral velocity com-

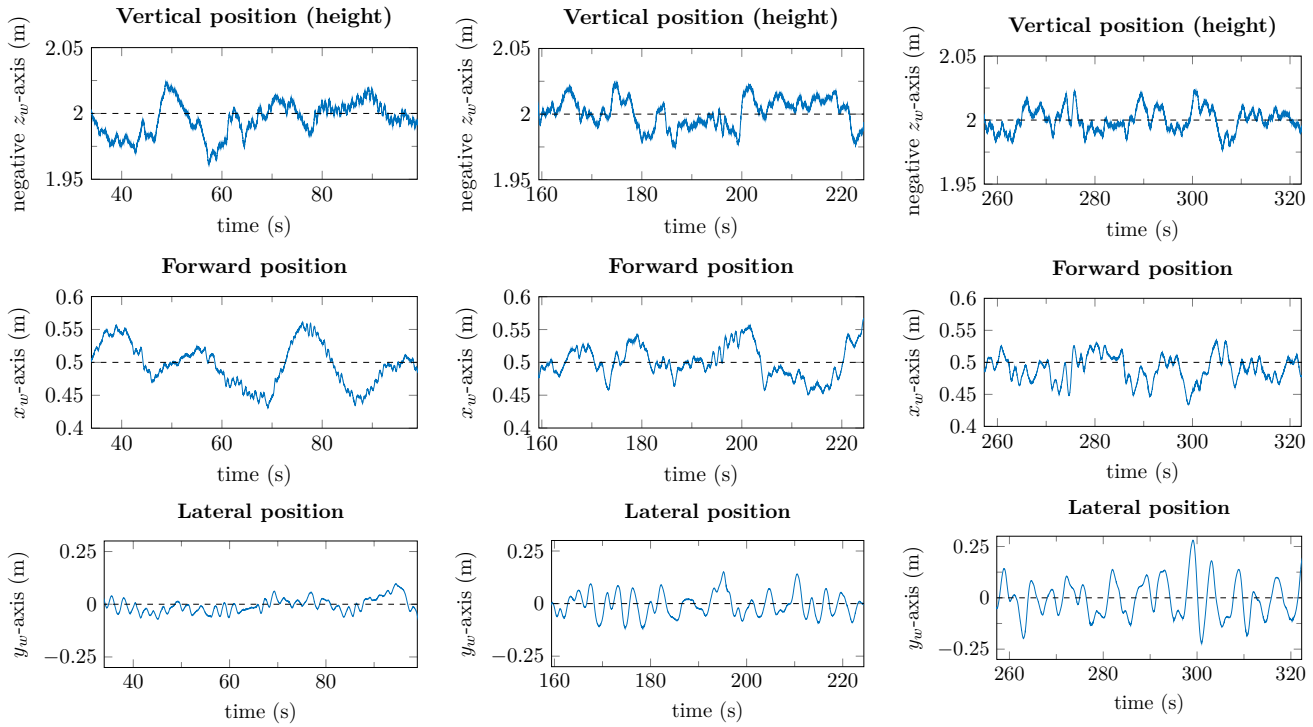

(a) Wind speed $V_W^{SP} = 0.7\,\mathrm{m/s}$. (b) Wind speed $V_W^{SP} = 1.0\,\mathrm{m/s}$. (c) Wind speed $V_W^{SP} = 1.3\,\mathrm{m/s}$.

Figure 9: Results for different wind speeds. (*semi-adaptive speed-thrust control with* $k = 0$, $i = 200\,\%$.)

ponent, the lateral control loop as third-order integrator system is more sensitive to increased wind speed and thus airspeed and pitch angle. By gain scheduling or dynamic inversion control, these couplings can be taken into account.

4.3 Height steps for different poles

The gains $d_{\ddot{H}z_w}, k_{\ddot{H}z_w}$ of the guidance control law are determined by the desired poles of the closed loop

$$\left(s^2 + d_{\ddot{H}z_w} s + k_{\ddot{H}z_w}\right) z_w(s) = \left(s - \varsigma_{z1}\right)\left(s - \varsigma_{z2}\right) z_w(s) = 0 \tag{16}$$

that is,

$$d_{\ddot{H}z_w} = -\varsigma_{z1} - \varsigma_{z2} \tag{17}$$

$$k_{\ddot{H}z_w} = \varsigma_{z1}\varsigma_{z2} \tag{18}$$

Desiring a "smooth" approach without overshoot, we chose pole pairs $\varsigma_{z1,2} \in \{-1, -3, -5\}$ on the left-hand real axis. The step responses for these pole pairs were tested in a flight arena where the DelFly flew at constant forward speed in circles with radii of 2 m, simulating the wind tunnel flight. The step responses are compared in Fig. 10.

The system response is as fast as desired and without overshoot beyond the accuracy of 2.5 cm for all three pole pairs; for the later pairs however, there is an initial deadband with a succeeding steeper rise indicating a delayed reaction of the underlying controller.

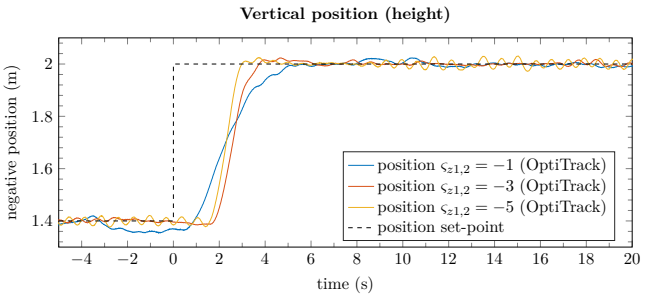

Figure 10: Height step response for different guidance poles, $\varsigma_{z1,2} \in \{-1, -3, -5\}$.[2]

5 Conclusion

We performed the first high-precision flight of a flapping-wing micro air vehicle in a wind-tunnel, maintaining an accuracy of ± 5 cm in all axes for most of the time; in the vertical axis in particular, we achieved an accuracy of ± 2.5 cm and below, up to ± 1 cm for tens of seconds. This performance both in position accuracy and in duration is more than sufficient in order to perform time-resolved stereo PIV.

Although the controller was tuned for a single wind speed (0.8 m/s), the longitudinal performance remained unaffected

[2] For $\varsigma_{z1,2} = -1$, the height set-point $H^{SP}(t < 0)$ was just below 1.4 m.

for the whole speed range tested (0.7 to $1.3\,\mathrm{m/s}$). The performance of the separated lateral controller decreased for higher speeds. This should be improved by gain scheduling or by dynamic inversion that take into account the roll and yaw coupling effects and the varying rudder effectiveness with speed. In addition—thanks to the modular design of the controller—the precision can be further improved by a fully-adaptive speed-thrust controller as well as by augmented filtering of position and attitude data originating from the off-board motion tracking and on-board inertial measurement.

To conclude, despite the lack of an accurate model of the DelFly MAV over its full flight envelope, we solved the flapping-wing position control problem successfully and, furthermore, in a new and advanced manner. Our work enables future investigations of the flapping wing aerodynamics *in-flight*, which should bring better understanding of the underlying aerodynamic mechanisms and result in advanced, more agile and more efficient flapping wing MAV designs.

REFERENCES

[1] M. Keennon, K. Klingebiel, H. Won, and A. Andriukov. Development of the Nano Hummingbird: A Tailless Flapping Wing Micro Air Vehicle. In *50th AIAA Aerospace Sciences Meeting including the New Horizons Forum and Aerospace Exposition*, Nashville, US-TN, Jan. 2012. American Institute of Aeronautics and Astronautics.

[2] K. Y. Ma, P. Chirarattananon, S. B. Fuller, and R. J. Wood. Controlled Flight of a Biologically Inspired, Insect-Scale Robot. *Science*, 340(6132):603–607, 2013.

[3] G. C. de Croon, K. M. de Clercq, R. Ruijsink, B. Remes, and C. De Wagter. Design, Aerodynamics, and Vision-based Control of the DelFly. *International Journal of Micro Air Vehicles*, 1(2):71–97, 2009.

[4] T. Nakata, H. Liu, Y. Tanaka, N. Nishihashi, X. Wang, and A. Sato. Aerodynamics of a Bio-inspired Flexible Flapping-wing Micro Air Vehicle. *Bioinspiration and Biomimetics*, 6, 2011.

[5] S. Deng, T. Xiao, B. van Oudheusden, and H. Bijl. Numerical Investigation on the Propulsive Performance of Biplane Counter-flapping Wings. *International Journal of Micro Air Vehicles*, 7(4):431–440, Dec. 2015.

[6] G. K. Taylor and A. L. R. Thomas. Dynamic Flight Stability in the Desert Locust *schistocerca gregaria*. *The Journal of Experimental Biology*, 206:2803–2829, 2003.

[7] J.-S. Lee and J.-H. Han. Experimental Study on the Flight Dynamics of a Bioinspired Ornithopter: Free Flight Testing and Wind Tunnel Testing. *Smart Materials and Structures*, 21, 2012.

[8] C. Rose and R. S. Fearing. Comparison of Ornithopter Wind Tunnel Force Measurements with Free Flight. In *IEEE International Conference on Robotics and Automation*, pp. 1816–1821, Hong Kong, CN, 2014. Institute of Electrical and Electronics Engineers.

[9] J. V. Caetano, M. Percin, B. W. van Oudheusden, B. D. W. Remes, C. De Wagter, G. C. H. E. de Croon, and C. C. de Visser. Error analysis and assessment of unsteady forces acting on a flapping wing micro air vehicle: free flight versus wind-tunnel experimental methods. *Bioinspiration & biomimetics*, 10(5):056004, Oct. 2015.

[10] S. K. Ghosh, C. L. Dora, and D. Das. Unsteady Wake Characteristics of a Flapping Wing through 3D TR-PIV. *Journal of Aerospace Engineering*, 25(4):547–558, Oct. 2012.

[11] H. Ren, Y. Wu, and P. G. Huang. Visualization and characterization of near-wake flow fields of a flapping-wing micro air vehicle using piv. *Journal of Visualization*, 16(1):75–83, 2013.

[12] M. Percin, B. W. van Oudheusden, H. E. Eisma, and B. D. W. Remes. Three-dimensional vortex wake structure of a flapping-wing micro aerial vehicle in forward flight configuration. *Experiments in Fluids*, 55(1806), 2014.

[13] S. Deng, M. Percin, and B. van Oudheusden. Experimental Investigation of Aerodynamics of Flapping-Wing Micro-Air-Vehicle by Force and Flow-Field Measurements. *AIAA Journal*, 54(2):588–602, 2016.

[14] H. Ben-Gida, A. Kirchhefer, Z. J. Taylor, W. Bezner-Kerr, C. G. Guglielmo, G. A. Kopp, and R. Gurka. Estimation of Unsteady Aerodynamics in the Wake of a Freely Flying European Starling (*sturnus vulgaris*). *PLoS ONE*, 8(11), 2013.

[15] F. T. Muijres, L. C. Johansson, Y. Winter, and A. Hedenström. Leading Edge Vortices in Lesser Long-nosed Bats Occurring At Slow But Not Fast Flight Speeds. *Bioinspiration and Biomimetics*, 9, 2014.

[16] P. Henningsson, D. Michaelis, T. Nakata, D. Schanz, R. Geisler, A. Schröder, and R. J. Bomphrey. The complex aerodynamic footprint of desert locusts revealed by large-volume tomographic particle image velocimetry. *Journal of the Royal Society Interface*, 12(108), 2015.

[17] C. De Wagter, A. Koopmans, G. C. de Croon, B. Remes, and R. Ruijsink. Autonomous Wind Tunnel Free-Flight of a Flapping Wing MAV. In *Advances in Aerospace Guidance, Navigation and Control*, pp. 603–621. Springer, Berlin, DE, 2013.

[18] J. Nowak. *Windkanal-Freiflugmessungen zur Bestimmung flugmechanischer Kenngrößen*. PhD thesis, RWTH Aachen University, Aachen, DE, 2010.

[19] J. N. Wiken. *Analysis of a Quadrotor in Forward Flight*. Master's thesis, Massachusetts Institute of Technology, Cambridge, US-MA, 2015.

[20] X. Deng, L. Schenato, and S. S. Sastry. Flapping Flight for Biomimetic Robotic Insects: Part II – Flight Control Design. *IEEE Transactions on Robotics*, 22(4):789–803, 2006.

[21] D. B. Doman, M. W. Oppenheimer, and D. O. Sigthorsson. Wingbeat Shape Modulation for Flapping-Wing Micro-Air-Vehicle Control During Hover. *Journal of Guidance, Control, and Dynamics*, 33(3):724–739, 2010.

[22] S. B. Fuller, M. Karpelson, A. Censi, K. Y. Ma, and R. J. Wood. Controlling Free Flight of a Robotic Fly Using an Onboard Vision Sensor Inspired by Insect Ocelli. *Journal of the Royal Society Interface*, 11, 2014.

[23] L. Roberts, H. Bruck, and S. Gupta. Modeling of Dive Maneuvers in Flapping Wing Unmanned Aerial Vehicles. In *2015 IEEE International Symposium on Safety, Security, and Rescue Robotics*, p. 6, 2015.

[24] P. Chirarattananon, K. Y. Ma, and R. J. Wood. Single-loop control and trajectory following of a flapping-wing microrobot. In *2014 IEEE International Conference on Robotics and Automation (ICRA)*, pp. 37–44. Institute of Electrical and Electronics Engineers, May 2014.

[25] P. Chirarattananon, K. Y. Ma, and R. J. Wood. Perching with a robotic insect using adaptive tracking control and iterative learning control. *The International Journal of Robotics Research*, Feb. 2016.

[26] G. C. de Croon, M. Perçin, B. D. Remes, R. Ruijsink, and C. De Wagter. *The DelFly: Design, Aerodynamics, and Artificial Intelligence of a Flapping Wing Robot*. Springer, Dordrecht, NL, 2016.

[27] B. D. W. Remes, P. Esden-Tempski, F. van Tienen, E. Smeur, C. D. Wagter, and G. C. H. E. de Croon. Lisa-S 2.8g Autopilot for GPS-based Flight of MAVs. In *IMAV 2014: International Micro Air Vehicle Conference and Competition*, pp. 280–285, Delft, NL, Aug. 2014.

[28] R. Brockhaus. *Flugregelung*. Springer, Berlin, DE, 2nd, revised edition, 2001.

[29] J.-J. Slotine and W. Li. *Applied Non-Linear Optimal Control*. Prentice-Hall, Upper Saddle River, US-NJ, 3rd edition, 1991.

[30] J. A. Koopmans and M. Karásek. Static force measurement of the Delfly flapping-wing MAV (*working title*). unpublished, 2015.

APPENDIX A: PROOF OF LEMMA 1

Proof. Let Θ_0, F_0, $\mathbf{F}_{Æ}$ be the true pitch angle, throttle command, and matrix of force gradients in equilibrium;

1. If the equilibrium condition is met, *i.e.* $\Theta^c = \Theta_0$, $F^c = F_0$, Eq. 15 yields

$$\begin{bmatrix} x'_w \\ H' \end{bmatrix} = \begin{bmatrix} x_{w0} \\ H_0 \end{bmatrix} + m^{-1}\hat{\mathbf{F}}_{Æ}\gamma^{-1} \begin{bmatrix} \Theta_0 - \hat{\Theta}_0 \\ F_0 - \hat{F}_0 \end{bmatrix} \tag{19}$$

   and $|x_{w0} - x'_w|$, $|H_0 - H'|$ are small for a suitable γ.

2. Let (x_w, H) be a position in the neighbourhood of the equilibrium (x'_w, H'); rearranging Eq. 19 yields

$$\begin{bmatrix} \Theta^c \\ F^c \end{bmatrix} = \begin{bmatrix} \hat{\Theta} \\ \hat{F} \end{bmatrix} + m\hat{\mathbf{F}}_{Æ}^{-1}\gamma \begin{bmatrix} x_{w0} - x'_w \\ H_0 - H' \end{bmatrix} = \begin{bmatrix} \Theta_0 \\ F_0 \end{bmatrix}$$

   and inserting into Eq. 15, we get

$$\begin{bmatrix} \Theta^c \\ F^c \end{bmatrix} = \begin{bmatrix} \hat{\Theta} \\ \hat{F} \end{bmatrix} + m\hat{\mathbf{F}}_{Æ}^{-1}\gamma \begin{bmatrix} x_{w0} - x'_w \\ H_0 - H' \end{bmatrix} + m\hat{\mathbf{F}}_{Æ}^{-1}\gamma \begin{bmatrix} x'_w - x_w \\ H' - H \end{bmatrix} = \begin{bmatrix} \Theta_0 \\ F_0 \end{bmatrix} + m\hat{\mathbf{F}}_{Æ}^{-1}\gamma \begin{bmatrix} x'_w - x_w \\ H' - H \end{bmatrix} \tag{20}$$

   Finally, recalling

$$\begin{bmatrix} \dot{V}_A \\ \ddot{H} \end{bmatrix} = m^{-1}\mathbf{F}_{Æ}(V_W) \left(\begin{bmatrix} \Theta \\ F \end{bmatrix} - \begin{bmatrix} \Theta_0 \\ F_0 \end{bmatrix} \right) \tag{21}$$

   and assuming $\Theta = \Theta^c, F = F^c$ we get

$$\begin{bmatrix} \dot{V}_A \\ \ddot{H} \end{bmatrix} = \mathbf{F}_{Æ}\hat{\mathbf{F}}_{Æ}^{-1}\gamma \begin{bmatrix} x'_w - x_w \\ H' - H \end{bmatrix} \tag{22}$$

   As $\hat{\mathbf{F}}_{Æ}$ is a close guess of $\mathbf{F}_{Æ}$, we can assume $\mathbf{F}_{Æ}\hat{\mathbf{F}}_{Æ}^{-1}$ is diagonal and positive; thus we have

$$\begin{aligned} \dot{V}_A &= \lambda_1\gamma\,(x'_w - x_w) \\ \ddot{H} &= \lambda_2\gamma\,(H' - H) \end{aligned} \tag{23}$$

   where $\lambda_1\gamma, \lambda_2\gamma > 0$ and the equilibrium position (x'_w, H') is stable in its neighbourhood.

□